Energy and angular distributions of 100- to 400-eV Na^+ scattered from Cu(110)

D. L. Adler and B. H. Cooper
Laboratory of Atomic and Solid State Physics, Clark Hall, Cornell University, Ithaca, New York 14853
(Received 8 October 1990)

In this paper we present a detailed analysis of the energy and angular distributions of 100-, 200-, and 400-eV Na^+ scattered from the Cu(110) surface. The spectra are analyzed using classical trajectory calculations with an improved ion-surface interaction potential. Qualitative features of the spectra can be reproduced using the chain model. Quantitative agreement between measured and simulated spectra is obtained with full-surface simulations, which include the thermal vibrations of the surface atoms. The trajectories are calculated using a potential constructed from a sum of $(Na-Cu)^+$ Hartree-Fock pair potentials plus an attractive interaction. At lower beam energies, the contribution to the scattering potential from the long-range tails of the pair potentials becomes increasingly important in determining the positions of the rainbow angles. The tails are also responsible for the dramatic increase in "focused" scattering events at lower beam energies. The simulations provide the impact parameters for the detected ions. This information is used to determine the relative importance of zigzag, focused, and top-layer chainlike scattering events. By examining the trajectories of ions scattered into the forward and backward rainbow angles, the extreme sensitivity of the backward rainbow peak to surface thermal vibrations is explained. Lastly, angular spectra from chain and full-surface simulations are compared.

I. INTRODUCTION

Low-energy ion scattering, with beam energies of several hundred eV to several keV, is a widely used technique for studying single-crystal metal surfaces.[1] The energy and angular distributions of the scattered ions depend on the potential between the incident ion and the surface,[2–7] the surface geometry,[8–13] the thermal vibrations of the surface atoms,[14–17] and the neutralization probabilities of the scattered species.[18] Good agreement between measured and simulated spectra can be achieved for keV ion scattering.[19] As the incident ion energy is lowered, changes in the ion-surface interaction are reflected in the scattered-ion distributions. Relatively few detailed studies have been made of scattering in the hyperthermal energy range (several eV to several hundred eV).[20–27] In this paper we present measured and simulated spectra for 100- to 400-eV Na^+ scattered from Cu(110).

The Cu(110) surface, whose geometry is shown in Fig. 1, has been investigated in previous scattering studies using keV ions. For example, Engelmann *et al.*[17] used 1-keV Ne^+ and Na^+ ions to study the thermal vibrations of the surface atoms. Their results were interpreted using full-surface simulations which employed a binary collision approximation to model the scattering. This model assumes that the ion interacts with only a single surface atom at a time.[3,28,29] Multiple scattering events are treated as successive binary collisions. Bronckers and De Wit have scattered 1-keV Ne^+ and H_2O^+ from this surface.[30] Their scattering results were interpreted using the binary collision approximation to calculate shadowing and blocking features in the scattered-ion distributions.

At the energies used in the present study, the incident ion may experience forces from several surface atoms simultaneously. Thus, to perform detailed comparisons with our data, we have replaced the binary collision model with trajectory simulations using the SAFARI computer code.[31] SAFARI uses an improved ion-surface interaction potential consisting of a sum of pair potentials[23–27,32,33] with an added attractive term to model the long-range ion-metal image potential.[33] Excellent agreement be-

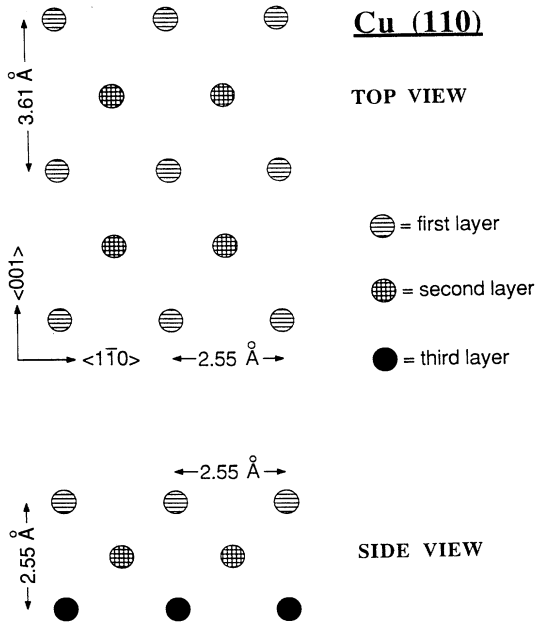

FIG. 1. Schematic top and side views of the Cu(110) surface.

tween measured and calculated energy and angular distributions is obtained using Hartree-Fock (HF) pair potentials calculated with GAUSSIAN86.[34] At incident ion energies of less than 500 eV, the calculated energy and angular ion distributions can be very sensitive to the shape of the scattering potential. We illustrate this below by comparing simulations using the HF pair potentials and the "universal" pair potential of Ziegler, Biersack, and Littmarck[35] (ZBL), which has been used to describe the scattering of Li^+, Na^+, and K^+ from Mo(001) in the energy range of 500–2500 eV.[6]

Having found a suitable potential, we then proceed to use the simulations to study in detail the scattered-ion trajectories. In particular, we examine the relative contributions to the spectra from focused and zigzag collisions, which depend both on scattering geometry and incident beam energy. Using SAFARI we can also investigate effects on the scattering trajectories from the thermal vibrations of the surface atoms, which are responsible for dramatic changes in the scattered-ion distributions.

This paper is organized into five main sections. In Sec. II we discuss the experimental details and sample preparation techniques. Section III describes the main features of SAFARI, including a brief discussion of the scattering potentials used in the simulations. Section IV reviews the chain model. The scattering results are presented in Sec. V, which contains subsections on our energy- and angle-resolved spectra, calculated impact parameter plots, a discussion of thermal effects, and the differences between the results of chain and full-surface simulations. Section VI summarizes our conclusions.

II. EXPERIMENT

A. Apparatus

The experimental apparatus is described in detail elsewhere.[36,37] Here we summarize the features that are relevant to the present work.

The beam line produces monochromatic beams ($\Delta E/E \leq 1\%$) of ions ranging in energy from approximately 10 eV to 10 keV. At the sample, a typical 100-eV beam has a diameter of less than 3 mm, a full angular divergence of 2°–4°, and a current of several nanoamps. At 400 eV, the beam has a diameter of 2 mm, an angular divergence of 2°, and a current in excess of 10 nA.[37] The UHV chamber is equipped with a sputter gun, rear-view low-energy electron diffraction (LEED), Auger spectrometer, residual gas analyzer, Kelvin probe, and getters for alkali-metal deposition. A sample manipulator provides x, y, and z translations, as well as sample rotation about three axes: azimuthal rotation about the sample normal, rotation of the sample normal in the scattering plane (described below), and rotation of the sample normal perpendicular to the scattering plane ("tilt"). For the experiments presented in this paper, the tilt rotation is used only to align the sample. The UHV scattering chamber has base pressures in the mid-10^{-11}-Torr range and typical operating pressures of $(1-2)\times 10^{-10}$ Torr.

The scattering plane is defined by the beam axis and the axis through the entrance apertures of the detector; these two axes intersect at the sample position (see Fig. 2). The total (laboratory) scattering angle of the detected particles is determined by rotating the detector in the scattering plane. Linear alignment between the beam-line optics, the detector, and the manipulator was achieved to about 0.25 mm, and angular alignment to within less than 0.5°.[36] The alignment was verified by collecting pairs of energy spectra with mirror symmetric scattering geometries. For all the scattering angles tested, the pairs of spectra agreed with one another to within our experimental precision.

The $\langle 1\bar{1}0 \rangle$ azimuth of the sample was aligned to within ±2° of the scattering plane using our LEED apparatus. The azimuthal position was then adjusted to within ±0.5° of the scattering plane by measuring scattered-ion intensities, which are very sensitive to small azimuthal rotations away from an axis of symmetry. Other azimuths can be chosen to ±0.5° accuracy using angular fiducial marks on the sample mount that can be seen from outside the vacuum chamber.

The scattered ions are energy analyzed using a 180° spherical electrostatic analyzer (ESA) with apertures chosen to give an energy resolution $\Delta E/E$ of 1% and an angular acceptance of ±1°. An energy spectrum is measured by ramping the voltage difference between the hemispheres, thus ramping the pass energy E of the analyzer. The particles transmitted by the ESA are detected by an electron multiplier operated in the pulse-counting mode. We have scaled each raw spectrum by a factor of $1/E$ to correct for the energy-dependent transmission function of the detector. The current on target is monitored continuously during an energy scan, so that any small changes in the incident ion beam current can be compensated for. Between spectra a Faraday cup, mounted below the sample on the sample manipulator, is placed at the sample position to measure the beam current. In practice this current is very stable, usually varying less than a few percent over several spectra. The Faraday cup is also used to monitor the beam diameter and position relative to the chamber center. The need to correct the spectra for different scattering geometries was avoided by keeping the illuminated spot on the sample smaller than the area imaged by the detector. It was

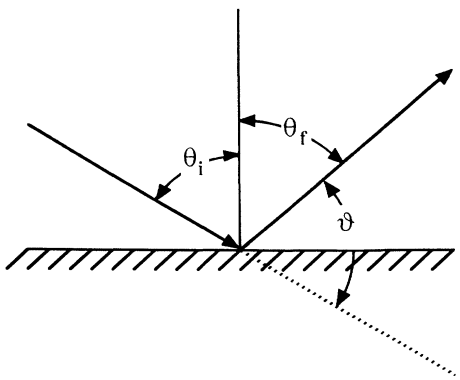

FIG. 2. Scattering geometry. $\theta_i = 55°$, θ_f is the final scattering angle, ϑ is the total scattering angle.

necessary, however, to correct for an incident ion dose-dependent neutralization effect. This is discussed in more detail in the next section.

B. Sample handling

The Cu(110) crystal[38] used in these measurements was cleaned using repeated sputter-anneal cycles described in detail elsewhere.[36] After the initial cleaning period, Auger spectra showed trace amounts of sulfur on the surface after prolonged annealing at 650 °C. Before each scattering experiment, in which 20–40 energy spectra were measured, we would uniformly sputter the sample with 1.5 μA of 500-eV Ar^+ ions for 30 sec, and then anneal the sample for 30 min at 550 °C. No sulfur was evident after the 30 min anneal. Good LEED patterns were achieved following this procedure. All the spectra presented in this paper were measured with the crystal near room temperature.

During data collection the sample was monitored for both surface damage and contamination from the alkali ion beam. The total beam dose per energy spectrum was on the order of 10^{12} alkali ions per mm^2. We saw no effects due to sputter damage from the incident beam. With long exposures to the beam, we observed a uniform decrease in the scattered-ion intensity, correlated with implantation of alkali ions in the surface. This attenuation was due to alkali-induced resonant charge transfer resulting in neutralization of the scattered ions, and did not depend significantly on the trajectory or final energy of the scattered particle.[39] The intensity decrease had a smooth and reproducible dependence on the total Na^+ dose to the crystal. The neutralization probability for a given dose increased with increasing energy of the incident ions, due to greater implantation rates. We monitored this intensity decrease by periodically measuring an energy spectrum at a fixed specular geometry of $\theta_i = \theta_f = 55°$, where θ_i and θ_f are the initial and final polar angles, respectively, measured with respect to the surface normal (see Fig. 2). The intensity decrease at this fixed geometry was used to correct the angular spectra for the increased-neutralization rates. In all cases, the corrections to the spectra were small, ranging from 2% or less at 100 eV to a maximum of 20% at 400 eV. The change in the neutralization rate during the accumulation of a single energy spectrum was insignificant.

III. SIMULATIONS

The scattered-ion trajectories are calculated with the program SAFARI. In the simulations presented in this paper we have approximated the ion-surface interaction potential as a sum of $(Na\text{-}Cu)^+$ pair potentials with an added attractive imagelike potential, which depends only on the perpendicular distance between the ion and the surface. The crystal used in the simulations is six layers deep and extends indefinitely in the plane parallel to the surface. The first- to second-layer spacing was contracted by 7.5% and the second- to third-layer spacing was expanded by 3.5% with respect to the bulk copper spacing, as determined from the medium energy ion scattering (MEIS) experiments of Copel *et al.*[40] Our results were insensitive to changes in the lattice spacing within the experimental uncertainty of Copel *et al.* ($\pm 1.5\%$). For each point in the trajectory the sum of pair potentials extends over the six surface atoms closest to the incident ion. Increasing either the number of layers representing the crystal or the number of atoms with which the incident ion interacts did not affect the calculated trajectories.

We have used several methods for calculating the $(Na\text{-}Cu)^+$ pair potential. In this paper, we discuss pair potentials calculated using the analytic formula for the Ziegler-Biersack-Littmarck[35] "universal potential," and a Hartree-Fock calculation.[33] In addition to the sum of pair potentials, our ion-surface potential includes the attractive imagelike term

$$V(z)=\begin{cases}\dfrac{-e^2}{4[z^2+(e^2/4V_{\min})^2]^{1/2}} & \text{if } z>0\\ -V_{\min} & \text{if } z\le 0,\end{cases}$$

where we have taken $z=0$ to lie in the top-layer plane of atoms. (At the energies discussed in this paper, the scattered-ion distributions are not significantly affected by changes in the location of the $z=0$ plane of the attractive interaction.) In Sec. V below, we will explore the effect of changing the saturation value $V_{\min}$ of the attractive term in the potential.

SAFARI generates the incident ion impact parameters in one of two ways. For simulations which do not include thermal vibrations of the surface atoms ("nonthermal" simulations), SAFARI uses an adaptive grid technique[31] to choose the impact parameters. The energy and angle of the incident beam, and the position, resolution, and pass energy of the detector are chosen to match the experimental conditions. The adaptive grid technique then varies the density of impact parameters to obtain trajectories from all contributing parts of the unit cell. Thus there will be very few impact parameters included for points in the unit cell corresponding to trajectories which do not scatter into the detector. The density of impact parameters chosen from regions of the unit cell which correspond to scattering into the detector is determined by how rapidly the final energy and angle of the scattered particle change with small variations in the impact parameter. The density is largest for those parts of the unit cell for which the final energies and angles are changing most rapidly, and is lowest for impact parameters producing scattering into the rainbow angles (see below), where the final energy and angle change slowly as a function of impact parameter.

The adaptive grid technique is very efficient for nonthermal simulations, but is not very efficient for thermal simulations. For thermal simulations, we use a Monte Carlo routine to generate both the impact parameters of the incident ions, and the initial positions and velocities of the surface atoms, which are chosen from a thermal distribution of Einstein oscillators. For most of the thermal simulations presented in this paper, we have used surface spring constants equal to those of the bulk, corresponding to rms vibration amplitude of 0.07 Å at room

temperature.[33] We have also performed some thermal calculations using the enhanced surface thermal vibrations suggested by Copel *et al.*[40] These (isotropic) thermal vibrations have rms amplitudes 50% larger than those for the bulk. As we will illustrate in Sec. V A, varying the surface thermal vibrations by this amount does not affect the peak positions significantly, but does affect the peak widths and background intensities.

SAFARI calculates and stores in a single file the impact parameter, final energy, and final angle for each trajectory. A separate detection program is then used to sort out those trajectories appropriate to the experimental scattering geometry for a given energy or angular spectrum. The detection program offers the options of choosing either a "spot" detector, centered at some polar and azimuthal final angle, or a "wedge" detector, which uses a fixed azimuthal angle and a range of final polar angles. For the simulations presented in this study, the energy resolution was fixed at 1% and the angular resolution at $\pm 2°$. This angular resolution is larger than our actual detector resolution by about a factor of 2. This difference is intended to compensate for the angular divergence of the incident beam ($\pm 1°$), which has not been included in the simulations.

In addition to calculating energy and angular spectra, the detection routine can also generate impact parameter plots for those trajectories which fall into the (simulated) detector. These plots are very helpful for classifying the scattering trajectories from different regions of the unit cell, as described in Sec. V B.

IV. CHAIN SIMULATIONS

Before we present the measured spectra, it is useful to lay the groundwork for discussing these data by reviewing the "chain model" of ion scattering.[16,41–43] This relatively simple model qualitatively describes some of the important scattering processes. In the chain model, trajectories are calculated from a set of impact parameters which are restricted to lie along a chain of atoms parallel to the scattering plane. (Focused and zigzag trajectories, which have impact parameters not along a chain of atoms, will be discussed in the next section.) In the chain calculations presented here, we use the full-surface potential to calculate the scattered-ion trajectories, i.e., the potential includes forces from neighboring atoms not in the scattering plane. Figure 3 shows calculated trajectories for 100-eV Na^+ with impact parameters along a top-layer $\langle 1\bar{1}0 \rangle$ chain of atoms on the Cu(110) surface. The scattering potential is a sum of Hartree-Fock pair potentials with an added imagelike potential, as described above. The thermal vibrations of the surface atoms have not been included in this calculation. The beam is incident at 55° from the surface normal and the evenly spaced impact parameters span one unit cell (2.55 Å) along the $\langle 1\bar{1}0 \rangle$ chain. The trajectories labeled 0–9 have impact parameters which are given by

$$\mathbf{b} = \frac{n}{10}\mathbf{a} ,$$

where n is the number of the trajectory and $\mathbf{a}$ is a unit vector in the $\langle 1\bar{1}0 \rangle$ direction. The origin of the unit cell is taken to be at the center of a top-layer atom.

We first consider trajectory 3 in Fig. 3, which corresponds to a total scattering angle of 86.5°.[44] The ion associated with trajectory 3 undergoes a "quasisingle" collision, in which momentum is transferred primarily to the surface atom located at $\mathbf{b}=0$. The final energy of 49.7 eV is close to the kinematic value of 50.0 eV for a 100-eV Na^+ ion to scatter through 86.5° following a binary collision with a single copper atom.[45] As we move to larger impact parameters (trajectories 4 and 5), the ion scatters through a smaller total scattering angle (larger θ_f) following the initial collision with the surface copper atom at $\mathbf{b}=0$, with the consequence that the ion interacts more strongly with the next atom in the chain at $\mathbf{b}=2.55$ Å. This second collision deflects the ion away from the surface (e.g., trajectory 5). For larger impact parameters, the second collision (at $\mathbf{b}=2.55$ Å) causes the total scattering angle to increase (trajectory 6). The minimum total scattering angle ($\vartheta=58.2°$) defines the forward "rainbow angle," which coincides with impact parameter 5.5.[46] Note that trajectory 5.5 does not undergo a pure single collision, but has significant interactions with *two*

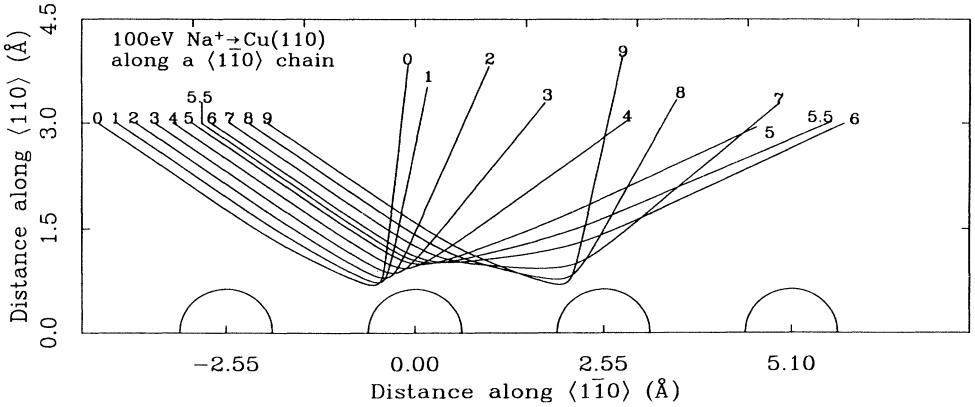

FIG. 3. Calculated trajectories for 100-eV Na^+ with impact parameters along a top-layer $\langle 1\bar{1}0 \rangle$ chain of atoms on the Cu(110) surface, $\theta_i = 55°$.

adjacent atoms in the chain.

As the impact parameter is increased further, the trajectory moves to larger total scattering angles (trajectories 6–8). Trajectories 7 and 8 represent "quasidouble" collisions, in which the ion undergoes two similar collisions with adjacent surface atoms at $\mathbf{b}=0$ and $b=2.55$ Å. These trajectories have total scattering angles similar to those of trajectories 3 and 4, but have larger final energies, as one would expect by considering the kinematics of single versus double collisions through a fixed scattering angle.[16,27]

Increasing the impact parameter past trajectory 9 results in less momentum transfer in the first collision at $\mathbf{b}=0$, and the trajectory becomes more like a quasisingle collision with the atom at $b=2.55$ Å. (Since the surface is periodic, impact parameter 10 is equivalent to impact parameter 0.) As the interaction with the first Cu atom decreases and that with the second copper atom increases, the total scattering angle reaches a maximum, and then begins to decrease. The maximum total scattering angle of 118.8° (trajectory 0) defines the backward "rainbow angle." As the impact parameter increases even further, as for trajectories 1 and 2, the total scattering angle decreases and the scattering is quasisingle again. The cycle then repeats, starting again with trajectory 3.

The scattering cycle can be summarized in an E-θ loop, in which the final energy and angle of each trajectory are plotted as the impact parameter is varied over one lattice constant.[16,42,43] Figure 4 shows the E-θ plot for the same scattering geometry as in Fig. 3. The solid line plots the final energy and angle as the impact parameter varies continuously over the chain of atoms. The numbered points on the loop correspond to the individual trajectories shown in Fig. 3. The E-θ loop may be described simply: as the impact parameter is varied along the chain, the point representing the final energy and angle of the corresponding trajectory moves along the E-θ loop. The motion of this point is periodic, i.e., it moves once around the loop as the impact parameter moves one unit cell along the chain. The trajectory at the forward rainbow (5.5) has the smallest total scattering angle (largest θ_f). The trajectory at the backward rainbow (0) has the largest total scattering angle (smallest θ_f). Between the two rainbows there exist two final energies for each final angle. The higher energy corresponds to a quasidouble collision, and the lower energy corresponds to a quasisingle collision.[16]

Energy-integrated angular spectra very clearly show the rainbow angles.[28,42] Figure 5 shows the angular spectrum corresponding to the 100-eV Na^+ (chain) E-θ loop of Fig. 4. The dashed and solid lines show the intensity of ions (with impact parameters along a $\langle 1\bar{1}0 \rangle$ chain) scattered from a surface with and without thermal vibrations, respectively. For the nonthermal simulation, the intensity reaches a maximum at the two rainbow angles, and drops abruptly to zero outside the rainbow angles. Between the rainbow angles, the intensity varies smooth-

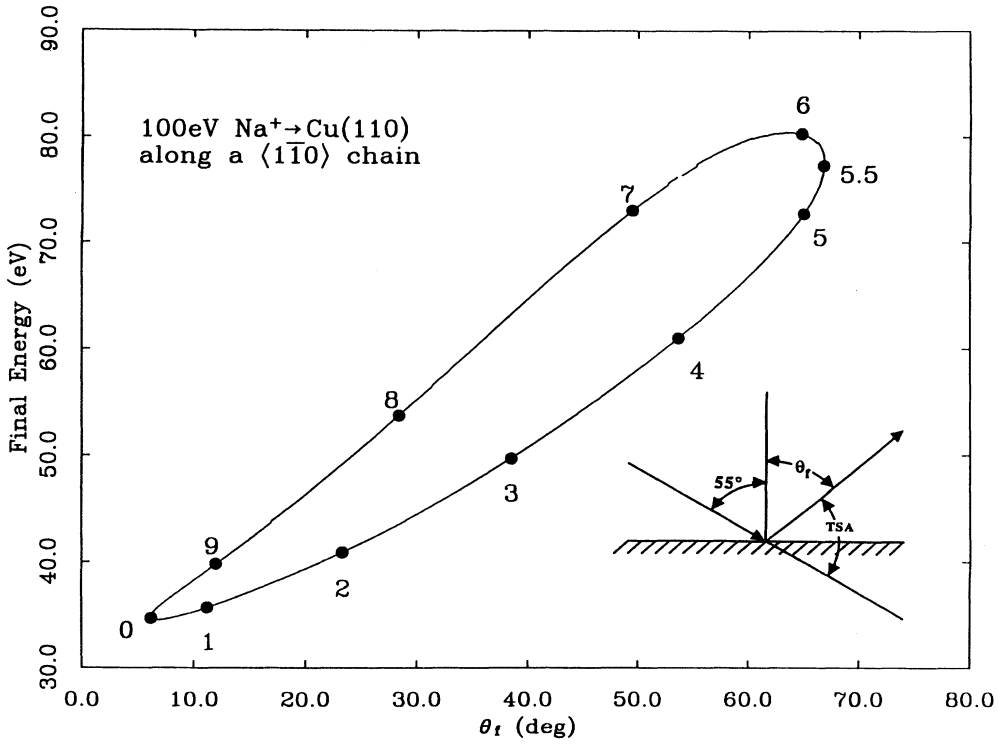

FIG. 4. A calculated E-θ loop showing the final energies and angles for 100-eV Na^+ ions scattered from a Cu(110) $\langle 1\bar{1}0 \rangle$ chain, as shown in Fig. 3. $\theta_i=55°$. The large solid points represent the final energies and angles of the trajectories shown in Fig. 3. The solid line represents the final energy and angle of the scattered ion as the impact parameter is continuously varied along the chain.

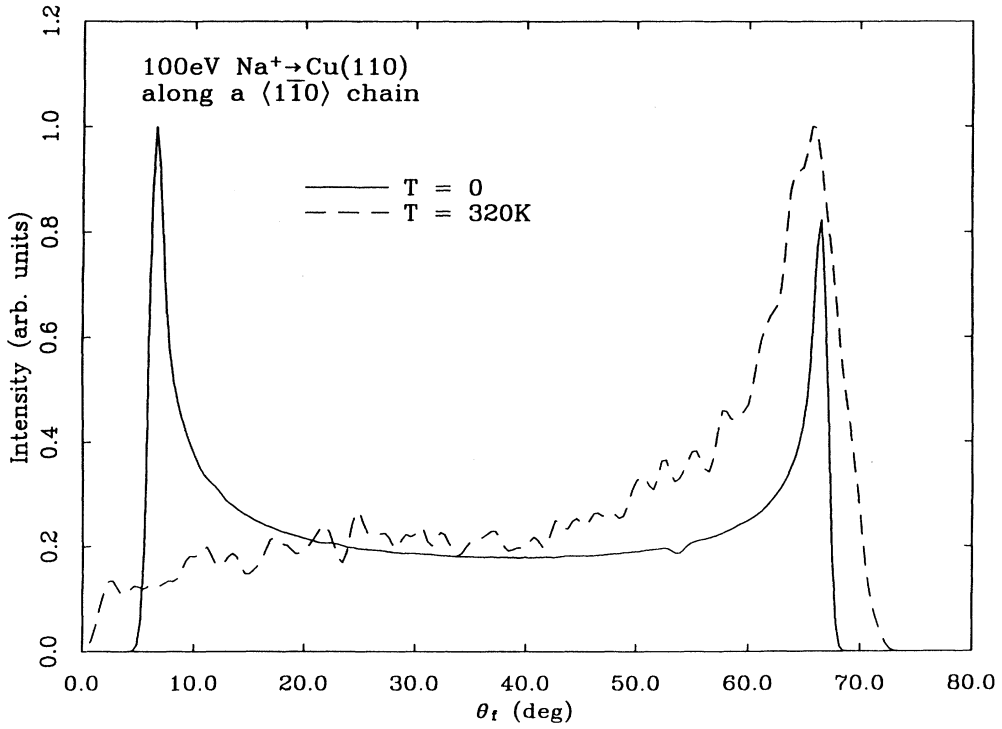

FIG. 5. Calculated angular spectra for the scattering as shown in Fig. 3. The final angle θ_f is measured from the surface normal. The solid line is the result of a nonthermal simulation while the dashed line is the result of a thermal simulation (see text).

ly between the two maxima. The thermal angular spectrum shows no backward rainbow peak. This effect is the subject of Sec. V C.

V. RESULTS

A. Spectra

Scattered-ion spectra can include significant contributions from trajectories not represented in chain calculations.[47] Even so, the chain model provides a convenient starting point for interpreting our measured spectra. Quasisingle and quasidouble scattering events dominate our measured energy spectra, and the rainbow angles are clearly seen in both our energy and angular spectra. In this section, we compare our measured spectra with full-surface thermal simulations. In particular, we will examine the sensitivity of our calculated spectra to changes in the scattering potential.

We begin with a qualitative comparison of measured and calculated energy spectra. Figure 6(a) shows a series of measured energy spectra for different final angles θ_f. The beam of 100-eV Na^+ is incident at 55° from normal along the ⟨1$\bar{1}$0⟩ azimuth of the Cu(110) surface. Each spectrum in Fig. 6(a) may be thought of as the scattered-ion intensity along a vertical line (fixed θ_f) in Fig. 4 (keeping in mind that Fig. 4 was generated from a chain simulation). For most of the scattering angles shown in Fig. 6(a) the energy spectra show two peaks, corresponding to quasisingle and quasidouble scattering events. The two peaks merge at the rainbow angles: the forward rainbow is between $\theta_f = 61°$ and 64°, and the backward rainbow is near $\theta_f = 22°$. While the forward rainbow shows a local intensity maximum, the backward rainbow does not. This effect, due to thermal vibrations, will be explored in Sec. V C.

Using a full-surface thermal simulation, we can calculate energy spectra corresponding to our experiments. Figures 6(b) and 6(c) show the results of two such calculations, for the same geometry and beam energy as in Fig. 6(a). The calculations were based on the Hartree-Fock pair potential described in Sec. III. The energy spectra in Fig. 6(b) were calculated using 50% enhanced surface thermal vibrational amplitudes,[40] while those in Fig. 6(c) were calculated using bulk vibrational amplitudes. The calculated spectra show the same two-peak structure seen in the data, although the intensities and widths of the two peaks differ considerably from each other and from the data. For the beam energies used in this paper, the calculated peak energies are only weakly dependent on the thermal motions of the surface atoms and the detector resolution. Changing the vibrational amplitudes [Figs. 6(b) and 6(c)] does not shift the peak positions significantly (less than 1%). By contrast, the relative intensities of the quasisingle and quasidouble peaks, as well as the background intensity between these peaks, are fairly sensitive to the thermal motions and the detector resolution. In this section we are primarily interested in information about the scattering potential as determined from the peak positions. We therefore defer any further

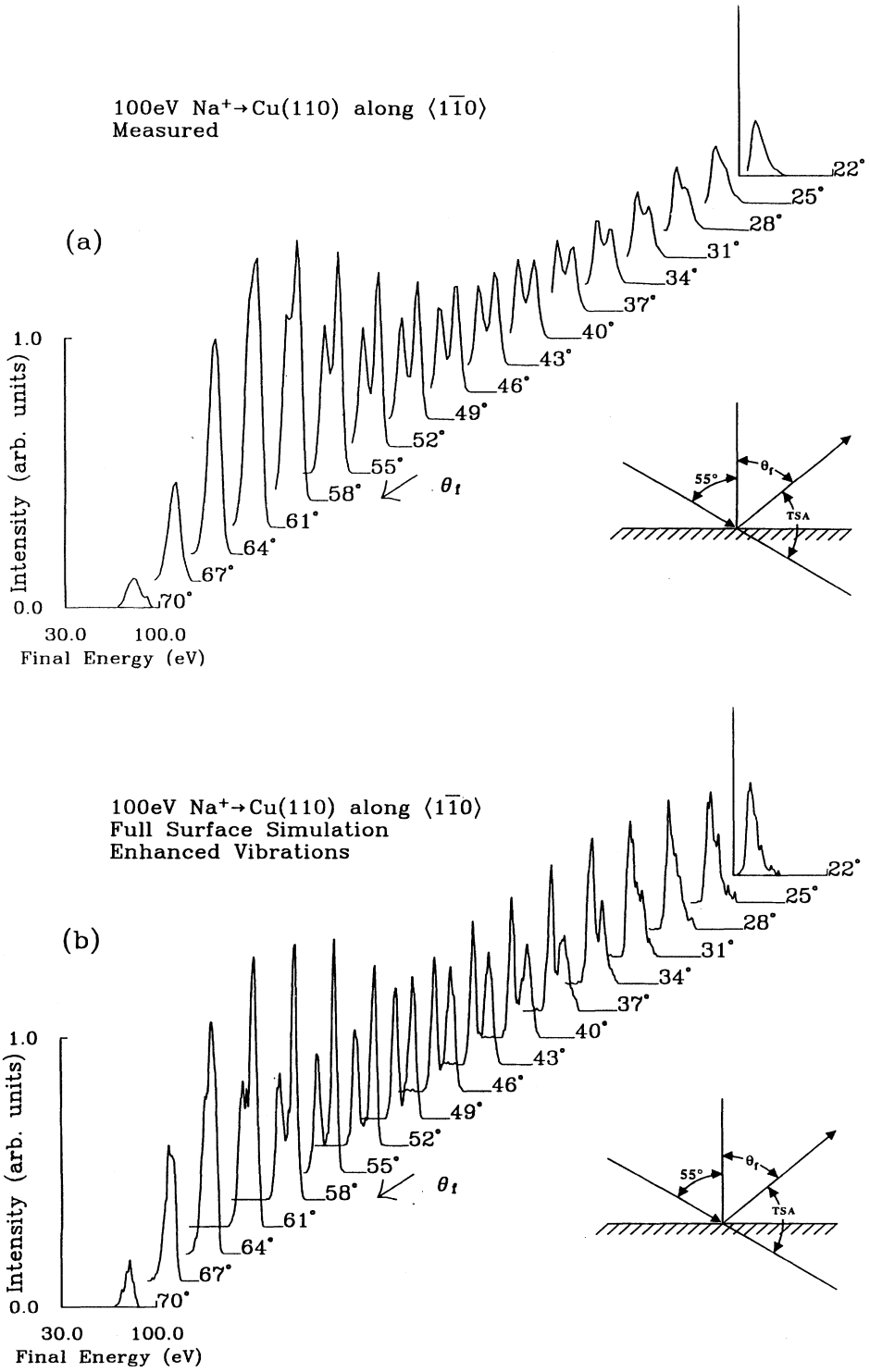

FIG. 6. (a) Measured energy spectra for different final angles θ_f. The 100-eV Na^+ beam is incident at $\theta_i = 55°$ from the surface normal, along the $\langle 1\bar{1}0 \rangle$ azimuth of the Cu(110) surface. The intensities have been corrected for the $1/E_f$ energy dependence of the transmission function of the analyzer. (b) Calculated energy spectra corresponding to the same scattering geometries as in (a), using enhanced surface thermal vibrations (see text). The saturation value V_{min} of the attractive term in the potential is 3 eV. The HF $(Na\text{-}Cu)^+$ pair potential was used. (c) Same as (b), but with bulk thermal vibrations (see text).

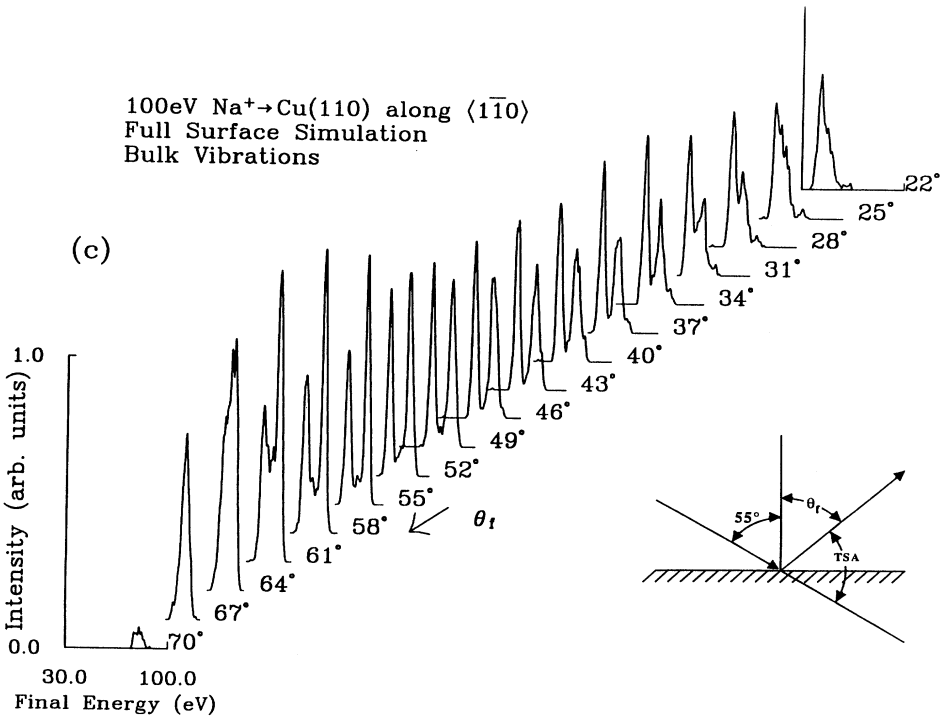

FIG. 6. (*Continued*).

discussion of thermal effects until Secs. V B and V C.

While the peak positions in the energy spectra are not very sensitive to changes in the surface atom vibrational amplitudes, they are very sensitive to the surface geometry and the scattering potential. This is illustrated by the E-θ loops in Figs. 7(a), 7(b), and 7(c) in which we compare peak positions from calculated energy spectra with the peak positions determined from the measured energy spectra shown in Fig. 6(a).[48] Figure 7(a) shows the peak positions determined from the energy spectra shown in Fig. 6(c), using the HF pair potential and $V_{\min}=3$ eV (see Sec. III). The agreement between measured and calculated peak positions is excellent. Figures 7(b) and 7(c) show calculated peak positions based on the Ziegler-Biersack-Littmarck pair potential. The E-θ loops in Figs. 7(b) and 7(c) correspond to values of $V_{\min}=4$ and 10 eV, respectively. Neither of the ZBL calculations reproduces the data as well as the HF-based calculation. (For a direct evaluation of the HF and ZBL potentials for modeling hyperthermal energy ion scattering, see Refs. 32 and 33.)

The E-θ loops depend on both the $(\text{Na-Cu})^+$ pair potential used and the depth of the image well $V_{\min}$. Comparing Figs. 7(b) and 7(c), we see that for similar values of $V_{\min}$, the ZBL potential generally produces higher final energies. This is because the ZBL pair potential is larger than the HF pair potential for large separations of the $(\text{Na-Cu})^+$ pair (see Fig. 8). The relatively large tails of the ZBL potential mean that distant surface atoms contribute more significantly to the scattering potential, thereby increasing the final energy of the scattered ion.

The additional repulsion of the ZBL potential can be somewhat compensated for by increasing the depth of the image well $V_{\min}$. Increasing $V_{\min}$ increases the acceleration of the ion toward the surface, resulting in a large energy loss in the scattering event. The ion then decelerates as it climbs out of the attractive well after scattering from the surface. Figure 7(c) shows the E-θ loop obtained with the ZBL pair potential and $V_{\min}=10$ eV. With this large value of $V_{\min}$, the ZBL E-θ loop shifts to energies more consistent with the measured peak positions. The separation of the forward and backward rainbow angles also increases when $V_{\min}$ is increased, since the image well affects the angular distribution as well as the energy distribution of the scattered ions.[49]

Increasing $V_{\min}$ improves the agreement between the ZBL-based calculation and the measured E-θ loop, but these changes are not sufficient to bring the ZBL pair potential into agreement with the data. Even with a large value of $V_{\min}$, the ZBL potential does not give good agreement between the measured and simulated positions of the quasisingle and quasidouble scattering peaks for large total scattering angles (small θ_f, see Fig. 9). For other scattering geometries and surfaces, it has been shown that at hyperthermal energies the ZBL pair potential cannot accurately reproduce measured spectra with any value of $V_{\min}$.[33]

The positions of the rainbow angles provide another test of the scattering potential.[26] Compare Figs. 7(a) and 7(b), which show HF- and ZBL-based calculations using

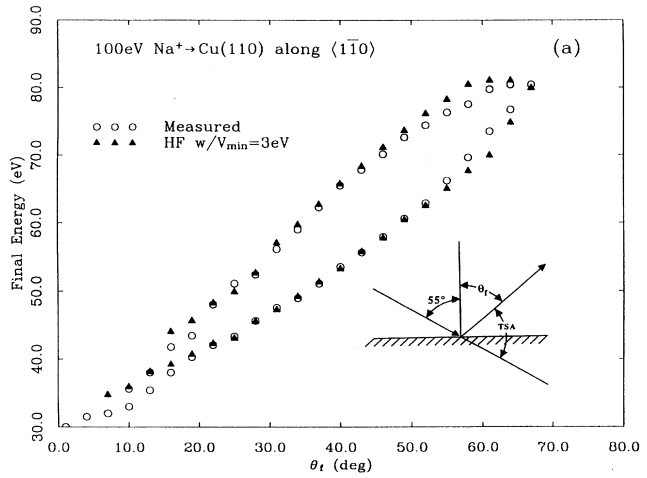

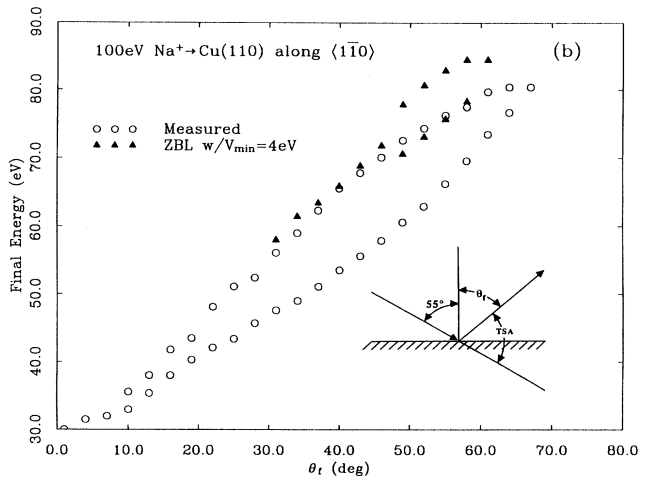

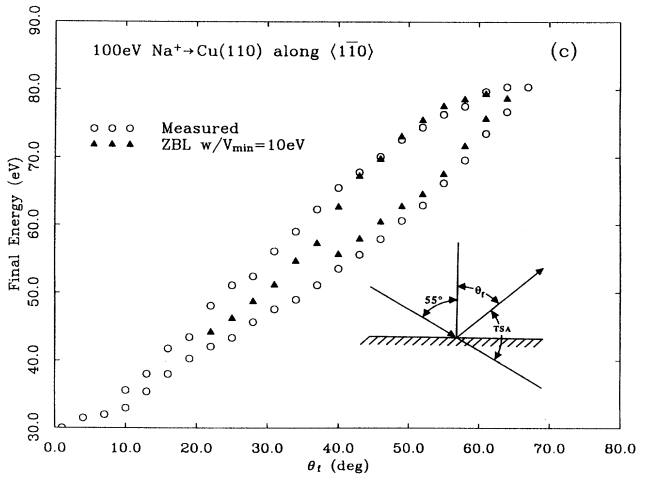

FIG. 7. (a) E-θ loops obtained from the measured and simulated peak positions of the energy spectra shown in Figs. 6(a) and 6(c). Near the forward rainbow angle, peak energies were determined by fitting a sum of two Gaussian functions to each spectrum. (b) Same as (a), but using the ZBL pair potential to calculate the scattering potential. $V_{min}=4$ eV. (c) Same as (b), but with $V_{min}=10$ eV.

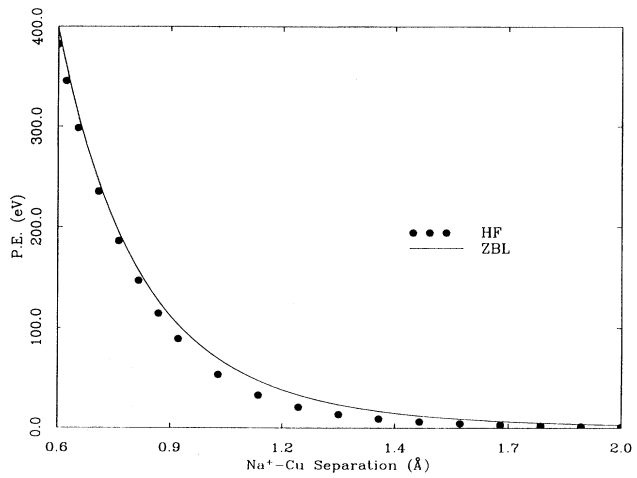

FIG. 8. Comparison of the HF and ZBL pair potentials as a function of the $(Na\text{-}Cu)^+$ separation.

similar values of V_{min}. The rainbow angles in the ZBL-based E-θ loop are much closer together than either the HF-based calculation or the measured values. This reflects the fact that the rainbow angles depend upon the "corrugation" of the ion-surface potential.[16] The larger this corrugation, the larger the angular separation of the rainbow angles. Following our discussion in the preceding section, this shift of the rainbow angle closer to the specular direction ($\theta_f=55°$) for the ZBL potential implies a smaller corrugation along the chain. This is again due to the relatively large "tails" of the ZBL potential. Since the data are accurately reproduced by the HF-based calculations, we conclude that, for this scattering geometry, the potential obtained in this way provides an accurate model of the surface corrugation.

A qualitative comparison of the HF and ZBL potentials can be obtained by comparing (energy-integrated) angular spectra. Figures 10(a), 10(b), and 10(c) compare

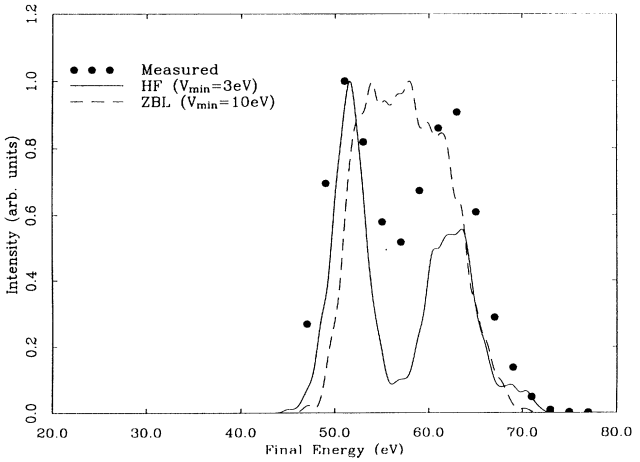

FIG. 9. Measured and calculated energy spectra of 100-eV Na^+ scattering from the Cu(110) surface along the ⟨1$\bar{1}$0⟩ azimuth, for $\theta_i=55°$, $\theta_f=37°$. The calculations use either the HF or ZBL pair potential, as indicated.

measured and simulated angular spectra using both HF- and ZBL-based potentials in the trajectory calculations. As discussed above, the ZBL calculation does not reproduce the measured forward rainbow position at 100 eV [Fig. 10(a)]. This is also true for 200 and 400 eV [Figs. 10(b) and 10(c)]. Because the potential is smoother for the ZBL calculation, the forward rainbow is closer to the specular direction ($\theta_f = 55°$) than for the HF calculation. As the beam energy is raised from 100 to 400 eV, the minimum separation between the ion and the surface atoms decreases. At small $(Na\text{-}Cu)^+$ separations, the difference between the HF and ZBL pair potentials decreases (see Fig. 8). Therefore angular spectra calculated with these two potentials become similar at higher energies, as indicated by Fig. 10(c).

The results presented above are not strongly dependent on how the surface thermal vibrations are modeled in our calculations. This is illustrated in Fig. 10(a), which shows an angular spectrum calculated using the HF pair potential with the enhanced surface thermal vibrations mentioned in Sec. III. Within the precision of the calculations, the two spectra are equivalent.

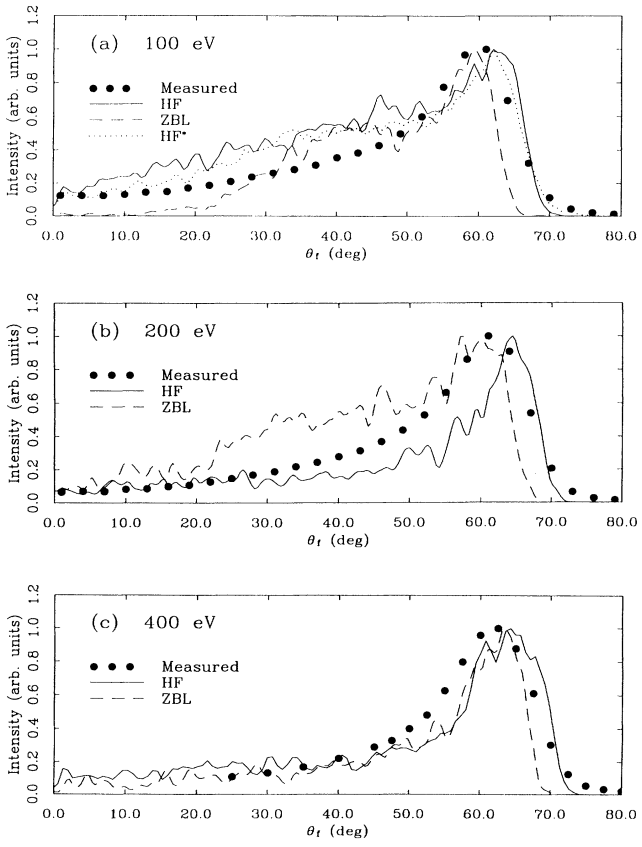

FIG. 10. Angular spectra for Na^+ scattering from the Cu(110) surface along the $\langle 1\bar{1}0 \rangle$ azimuth, for $\theta_i = 55°$. The HF and ZBL calculations use $V_{min} = 3$ and 10 eV, respectively. θ_f is measured from the surface normal. (a) 100-eV incident ion energy. The HF* simulation was performed using enhanced surface vibrations (see text). (b) Same as (a) for 200-eV incident ion energy. (c) Same as (a) for 400-eV incident ion energy.

B. Impact parameter plots and trajectories

In Sec. IV we plotted representative trajectories calculated from chainlike simulations. By definition, these trajectories correspond to impact parameters aligned with rows of surface atoms. At hyperthermal energies, only a small fraction of the scattered ions correspond to these chainlike scattering events.[27,30] In this section, we determine the relative importance of the different kinds of trajectories which make significant contributions to the observed spectra. In particular, we will study the focused and zigzag trajectories which scatter in the plane defined by the incident ion beam and the surface normal.

The strong focusing of ions by the Cu(110) surface has been discussed previously.[17,30] Focused trajectories result from impact parameters not quite directly above the second-layer chains of copper atoms. While ions with impact parameters slightly off a chain of top-layer atoms are scattered out of plane, ions with impact parameters slightly off a second-layer chain may still be scattered into the detector due to small-angle lateral collisions with top-layer atoms (see Fig. 11).[50,51] The final azimuthal angle for these focused trajectories is relatively insensitive to small lateral variations in the impact parameter. This focusing greatly enhances the contribution to the measured in-plane spectra from ions which scatter from the second layer into the detector.

Zigzag trajectories occur when ions experience two or more collisions, the first of which scatters the ion out of plane while the second scatters the ion back in plane.[5] Several types of zigzag trajectories can occur involving top- and second-layer atoms. They can produce identifiable new peaks, contribute to an overall background, or widen other peaks in the energy spectra. Focused trajectories may be thought of as zigzag trajectories with small lateral deflections.

The relative importance of focused and zigzag trajectories can be determined by examining the impact parameters for trajectories which contribute to a given spec-

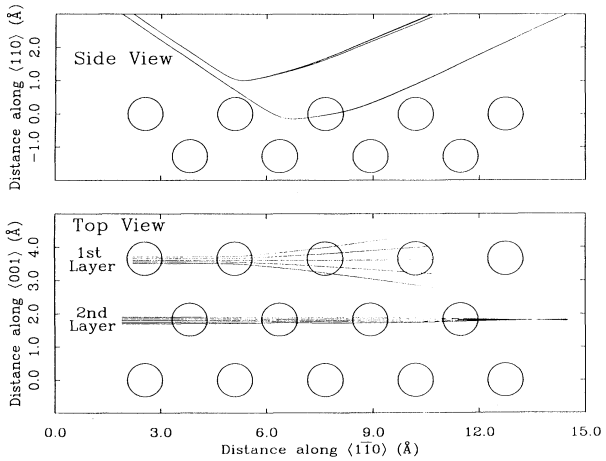

FIG. 11. Top and side views of calculated ion trajectories for 100-eV Na^+ scattering from the top and second layers along the $\langle 1\bar{1}0 \rangle$ azimuth of Cu(110), demonstrating the focusing effect along the second layer.

trum. We define the impact parameter for a given trajectory as the point at which the ion, if undeflected, would intersect a plane through the top layer of atoms. Each type of trajectory, i.e., quasisingle, zigzag, etc., will have a corresponding region of impact parameters in the unit cell. For the nonthermal surface (no thermal vibrations), these regions do not overlap. The scattering cross section for the detected ions coming from top-layer, second-layer, and zigzag collisions can be found by determining the fractions of the unit cell occupied by impact parameters corresponding to that type of event.

For a given choice of incident beam energy, crystal azimuth, and incident beam angle, SAFARI can generate impact parameter plots corresponding to any choice of final angle and energy for the scattered particles. Continuing our examination of 100-eV Na^+ scattering from Cu(110), incident at $\theta_i = 55°$ from normal along the $\langle 1\bar{1}0 \rangle$ azimuth (i.e., the same parameters as those used in Fig. 6), we first examine the impact parameters corresponding to ions which are scattered into the forward rainbow angle. To isolate these trajectories, SAFARI uses a "spot" detector whose center is located at $\theta_f = 65°$, which is the position of the forward rainbow angle as determined by chain simulations. The spot detector is $\pm 2°$ wide in both polar and azimuthal angles. The impact parameter plot corresponding to this detector is shown in Fig. 12. The thermal motions of the surface atoms are not included in this simulation.

The impact parameters for trajectories that scatter into the forward rainbow fall into several distinct regions within the surface unit cell. We have analyzed the trajectories corresponding to the impact parameters 1–4 in Fig. 12. These trajectories are shown in Figs. 13(a)–13(d). Impact parameter 1 in Fig. 12 is directly over the second-layer chain of atoms, and side and top views of the corresponding trajectory are shown in Fig. 13(a). As expected for scattering into the forward rainbow angle, the trajectory is not a clearly defined quasisingle or quasidouble collision. Figure 13(b) shows the focused collision corresponding to impact parameter 2, which is slightly to the side of the second-layer chain of atoms. The lateral deflections associated with this trajectory are very small on the scale of this figure. The ion first scatters out of plane and is then focused back into the plane of the detector by collisions with top-layer atoms on the outgoing trajectory. The trajectory is very nearly the same as for impact parameter 1. Figure 13(c) shows the side and top views of the trajectory associated with impact parameter 3 in Fig. 12. This trajectory scatters off the top-layer chain of atoms into the detector.

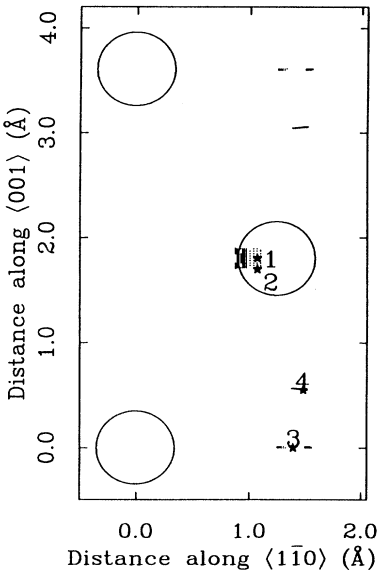

FIG. 12. Impact parameters corresponding to trajectories which scatter into the forward rainbow angle ($\theta_f = 65°$). The 100-eV Na^+ beam is incident from the left, at $\theta_i = 55°$, parallel to the $\langle 1\bar{1}0 \rangle$ direction. The figure depicts one unit cell, with top-layer atoms at $x = 0$ along the $\langle 1\bar{1}0 \rangle$ azimuth and a second-layer atom at $x = 1.275$ Å along the $\langle 1\bar{1}0 \rangle$ azimuth and $y = 1.803$ Å along the $\langle 001 \rangle$ azimuth. Thermal vibrations of the surface atoms are not included in this simulation.

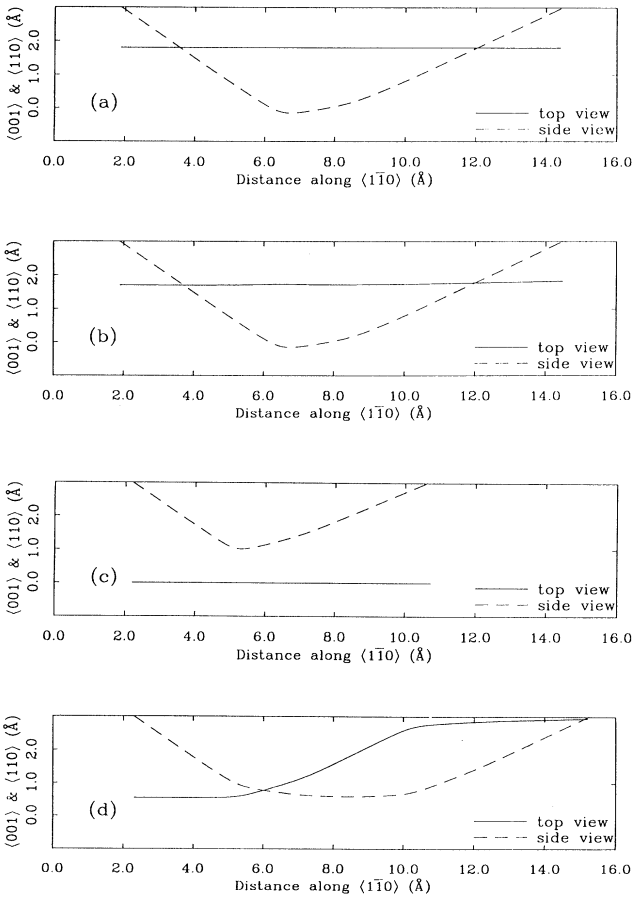

FIG. 13. Trajectories with impact parameters as labeled in Fig. 12. The solid (dashed) line represents the top (side) view of the trajectory. The scale is the same for both views: for the side view, distance along the y axis is perpendicular to the surface; for the top view, distance is along the $\langle 1\bar{1}0 \rangle$ azimuth. (a) Trajectory for an ion with the impact parameter labeled "1" in Fig. 12. (b) Trajectory "2." (c) Trajectory "3." (d) Trajectory "4."

The trajectory for impact parameter 4 is shown in Fig. 13(d). This is a "zigzag" trajectory whose impact parameter lies between the top- and second-layer rows of atoms. The ion collides with a top-layer atom, is deflected out of plane, passes over the second layer, and is deflected back into the scattered plane by an atom in a different top-layer chain.

As previously discussed, the position of the rainbow angles depends on the corrugation of the scattering potential.[16,41] This can be illustrated here by comparing the trajectories with impact parameters 1 and 3 [Figs. 13(a) and 13(c), respectively]. The forward rainbow angle for the second-layer chain (impact parameter 1) is a few degrees closer to the surface normal than for the top-layer chain (impact parameter 3). This is consistent with the fact that the scattering potential along the second-layer chains is smoother than the potential along the top-layer chains. Along a second-layer chain, the potential includes contributions from the second-layer atoms and from both top- and third-layer atoms. Along a top-layer chain, the potential includes only significant contributions from the top-layer atoms and from second-layer atoms. The potential along a second-layer chain is thus smoother than along a first-layer chain. The resulting second-layer rainbow angles are somewhat closer to the normal direction than for the top layer, i.e., θ_f is smaller for the forward rainbow.

Impact parameters in each region of the unit cell correspond to a particular type of scattering event. By repeating the above analysis for the entire unit cell, it is possible to map out the final angle for every impact parameter.[25,26] Instead, we will restrict our discussion to those impact parameters leading to ions which are scattered in plane and therefore contribute to the spectra shown in Fig. 6. For the scattering geometry used in Fig. 6, we have generated impact parameter plots for all ions that are scattered in plane. To do this SAFARI uses a wedge-shaped detector that spans scattering angles $-90° < \theta_f < +90°$, along the $\langle 1\bar{1}0 \rangle$ azimuth. Figure 14 shows the impact parameter plots generated using such a "wedge" detector for incident beam energies of 100, 200, and 400 eV. The density of points in the shaded regions varies with the rate of change of the final energy and angle of the scattered particles as the impact parameter is varied (see Sec. III). The density is lowest for impact parameters which contribute to the rainbow angles, where the final energy and angle change slowly with respect to the impact parameter. The atom positions in the first and second layer are shown as reference points. Due to the angle of the incident beam, the impact parameters for ions colliding with second-layer atoms appear 1.82 Å to the left of where the undeflected trajectories would pass through the second layer. Thus, for example, ions with impact parameters in region "II" of Fig. 14(a) would, if undeflected, pass almost directly through the second-layer atoms, while ions with impact parameters in the region labeled "I" would pass between second-layer atoms.

We have analyzed trajectories from each of the six labeled regions in Fig. 14(a), and identified them with focused, zigzag, or chainlike trajectories. Impact parameters producing focused trajectories occur along the second-layer chains, for example, regions I and II from Fig. 14(a). Region I, as can be seen in Fig. 12, corresponds to ions scattered into the forward rainbow. Region II corresponds to the backward rainbow. The impact parameters along the second-layer chain between re-

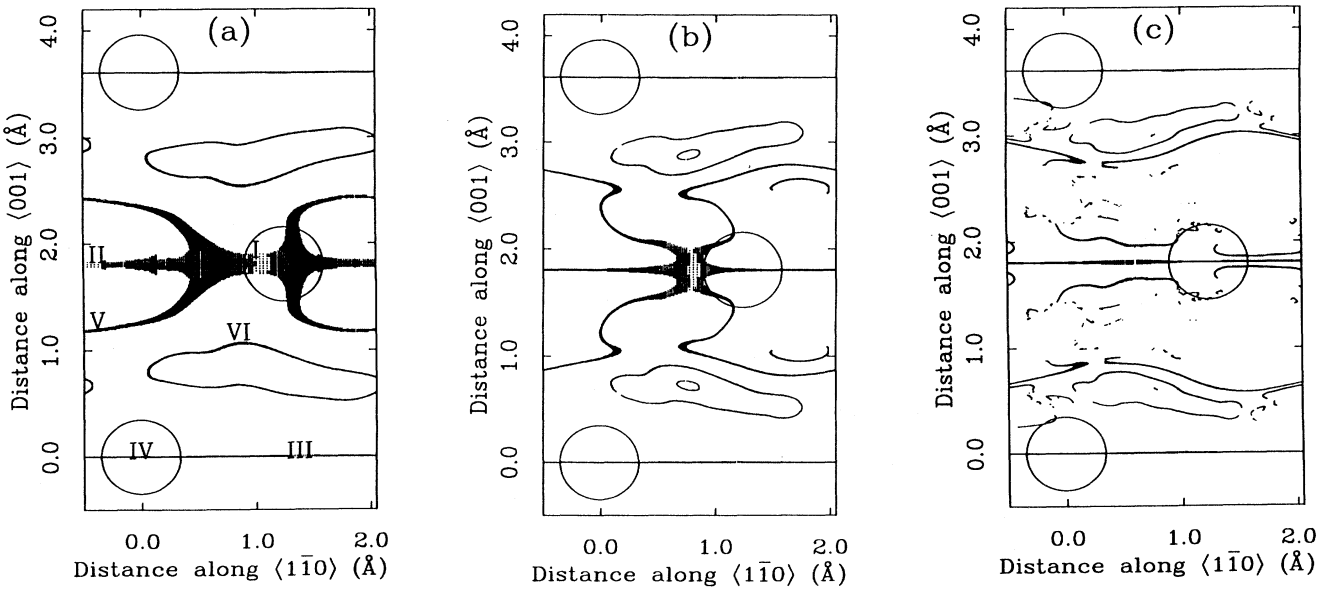

FIG. 14. Simulated nonthermal impact parameter plots (see text). The shaded regions correspond to impact parameters for trajectories scattered in plane. The beam is incident from the left at $\theta_i = 55°$, along the $\langle 1\bar{1}0 \rangle$ azimuth of Cu(110). The incident Na^+ beam energies are (a) 100 eV, (b) 200 eV, and (c) 400 eV.

gions II and I ($-0.3 < x < 1.0$) in Fig. 14(a) correspond to quasisingle scattering events, and the impact parameters to the right of region I ($1.0 < x < 2.25$) correspond to quasidouble scattering events.

In-plane scattering from a top-layer chain occurs for the impact parameters centered over the top-layer atom chains, such as those in regions III and IV of Fig. 14(a). The forward rainbow corresponds to impact parameters in region III, which lies between top-layer atoms, and the backward rainbow corresponds to region IV, which is directly over a top-layer atom. The impact parameters producing quasisingle collisions from a top-layer atom lie between regions IV and III ($0.0 < x < 1.3$), and the remaining impact parameters ($1.3 < x < 2.55$) result in quasidouble collisions. Note that for in-plane scattering, impact parameters corresponding to scattering from top-layer atoms span a narrow range along the $\langle 001 \rangle$ direction, while those corresponding to second-layer scattering span a relatively large range. This is a result of the focusing which occurs for second-layer scattering.

The zigzag scattering events for this surface can be classified into two types.[5] The first, with impact parameters in region VI, corresponds to zigzag trajectories which consist of sequential collisions off of two top-layer atoms which lie in different chains. The second type, with impact parameters in region V of Fig. 14(a), have a collision first with a top-layer atom and then a second-layer atom. The latter are not qualitatively different from the focused collisions of region II, since focusing involves small-angle collisions with the top layers. The second type of zigzag collision will be important when we discuss thermal effects.

The distribution of impact parameters for in-plane scattering is very sensitive to the incident ion energy. Figures 14(b) and 14(c) show impact parameter plots for 200- and 400-eV Na^+, with the same scattering geometry as for the 100-eV beam. In general, as the energy of the incident beam increases, the second-layer focusing decreases, which in turn decreases the relative importance of second-layer scattering. For ions scattered into the forward rainbow, however, the focusing actually increases as the energy goes from 100 to 200 eV, so that second-layer scattering becomes even more important in determining the rainbow angle. At 400 eV the focusing is greatly reduced, increasing the relative contributions from top-layer and zigzag trajectories.

While impact parameter plots derived from nonthermal simulations are very useful for determining the types of trajectories which contribute to the spectra, thermal simulations are required to accurately model the data.[17] Figures 15(a)–15(c) show impact parameter plots from simulations in which thermal vibrations have been included. The atoms are treated as Einstein oscillators with rms amplitude of 0.07 Å (see Sec. III). The initial positions and velocities of the surface atoms are chosen with a random Gaussian distribution consistent with a surface temperature of 320 K.[21] The other scattering parameters are the same as those used in Fig. 14. The simulation uses 70 000 impact parameters, selected at random in the unit cell. The impact parameter plot shows those impact parameters which scatter in-plane. While the features in Fig. 15(a) are not as well defined as those in Fig. 14(a), the basic structure is similar. The focusing is still apparent, as are some of the zigzag features. In agreement with the nonthermal results shown in Figs. 14(a)–14(c), the focusing for scattering into the forward rainbow angle is larger at 200 than at 100 eV, and decreases as the energy is raised to 400 eV. The top-layer scattering remains roughly the same as the beam energy is changed.

In the thermal calculations, the impact parameters corresponding to the focused and zigzag collisions of regions II and V overlap substantially. This smears out the structure in the angular spectra at large scattering angles. As we will see in the next section, backscattered ions (regions II and V) are much more sensitive than forward-scattered ions (region I) to the thermal vibrations of the surface atoms.

C. Thermal vibrations

In Fig. 5, we saw a very important consequence of the surface thermal vibrations. While the forward rainbow showed the expected intensity peak, the backward rainbow showed no intensity peak. The relatively high sensitivity of the backscattered rainbow (compared to the forward rainbow) to thermal vibrations has been previously noted by Poelsema *et al.* for keV scattering[15] and predicted by Gerlach-Meyer *et al.* for hyperthermal energy scattering.[21] The disappearance of the backward rainbow intensity peak can also be seen in our measured energy spectra (Fig. 6) and angular spectra (Fig. 10).

Thermal vibrations affect the rainbow angles by changing the relative positions of atoms along the chain. This is illustrated in Fig. 16, which shows E-θ loops calculated along different types of chains of atoms. The solid line is the E-θ loop for a nonthermal chain calculation over a second-layer $\langle 1\bar{1}0 \rangle$ copper chain. The dashed line is the E-θ loop for a second-layer chain in which every other copper atom has been displaced upward by 0.07 Å, producing a buckled chain. This buckling is chosen to mimic the thermally induced displacements along the chains of surface atoms. On the real surface, the average displacement between adjacent atoms is probably smaller due to correlated motions of adjacent atoms.[40]

The E-θ loop for the buckled chain (dashed line) consists of two connected loops due to the doubled length of the unit cell. The two pairs of rainbow angles can be thought of as resulting from the two effective incident angles as measured from the two local surface normals along the chain. In general, for any thermally induced displacement of neighboring atoms, there will be a shift in the effective incident angle, causing a corresponding shift in the forward and backward rainbow angles.[15] The dashed curve in Fig. 16 shows that the backward rainbow angle is much more sensitive than the forward rainbow angle to a change in the relative positions of the surface atoms.

On the real surface, the atoms have random thermal displacements, causing the rainbow angles to be distributed over a range of final scattering angles. We simulated this situation by performing a chain calculation with a

thermal surface, i.e., a chain of impact parameters over a second-layer $\langle 1\bar{1}0 \rangle$ chain of atoms with random displacements and velocities consistent with a surface at room temperature. The final energies and angles of 1000 ions with randomly chosen impact parameters over the chain are shown by the dots in Fig. 16. The forward intensity maximum is spread over about 7°, while there is no intensity maximum of backscattered ions.

The high sensitivity of the backward rainbow angle to thermal displacements of neighboring atoms can be understood by a simple physical argument. In Fig. 3, the trajectory scattered into the forward rainbow angle, trajectory 5.5, has relatively small-angle collisions with two surface atoms. Conversely, the trajectory scattered into the backward rainbow angle, trajectory 0, has a grazing angle collision followed by a hard, large-angle collision with a second surface atom. An ion scattered into the backward rainbow angle therefore comes much closer to a surface atom than an ion scattered into the forward rainbow angle. If there is a shift in the relative positions of neighboring atoms along the chain, the impact parameter of the ion with respect to the second collision is altered. For ions scattered into the forward rainbow angle, this small shift in the impact parameter causes a small change in the final angle. For the backscattered ions, however, a similar shift in the impact parameter of the second collision produces a much larger change in the final angle. This is because the trajectory of the ion is very sensitive to small changes in the impact parameter for small impact parameters. Backscattered ions are therefore more sensitive to thermal displacements of the surface atoms than forward-scattered ions.

D. Chain versus full-surface simulations

Lastly, it is of practical interest to compare a simulated full-surface angular spectrum with one obtained from a one-dimensional chain of impact parameters.[47] The chain simulation can be performed in 20% or less of the time required for a full-surface calculation, but ignores contributions to the spectra from zigzag or focused collisions. Figure 17 compares an angular spectrum for a second-layer thermal chain simulation (for the same scattering geometry used in Fig. 6) with the full-surface angular spectrum from Fig. 10. The leading edge of the forward rainbow in the full-surface simulation is accurately reproduced by the second-layer chain simulation. This is because the scattered-ion intensity at the forward rainbow is strongly dominated by focused scattering from the second layer, as discussed in the preceding section. At large scattering angles, contributions from zigzag and top-layer collisions cause differences between the chain and full-surface spectra.

VI. SUMMARY

We have presented measured and calculated in-plane energy- and angle-resolved scattered-ion distributions for 100–400-eV sodium ions incident along the $\langle 1\bar{1}0 \rangle$ azimuth of Cu(110). Qualitative features of the scattered-ion distributions were reproduced by chain calculations in which the impact parameters were restricted to lie along a top- or second-layer row of copper atoms. The scattering potential was constructed from a sum of

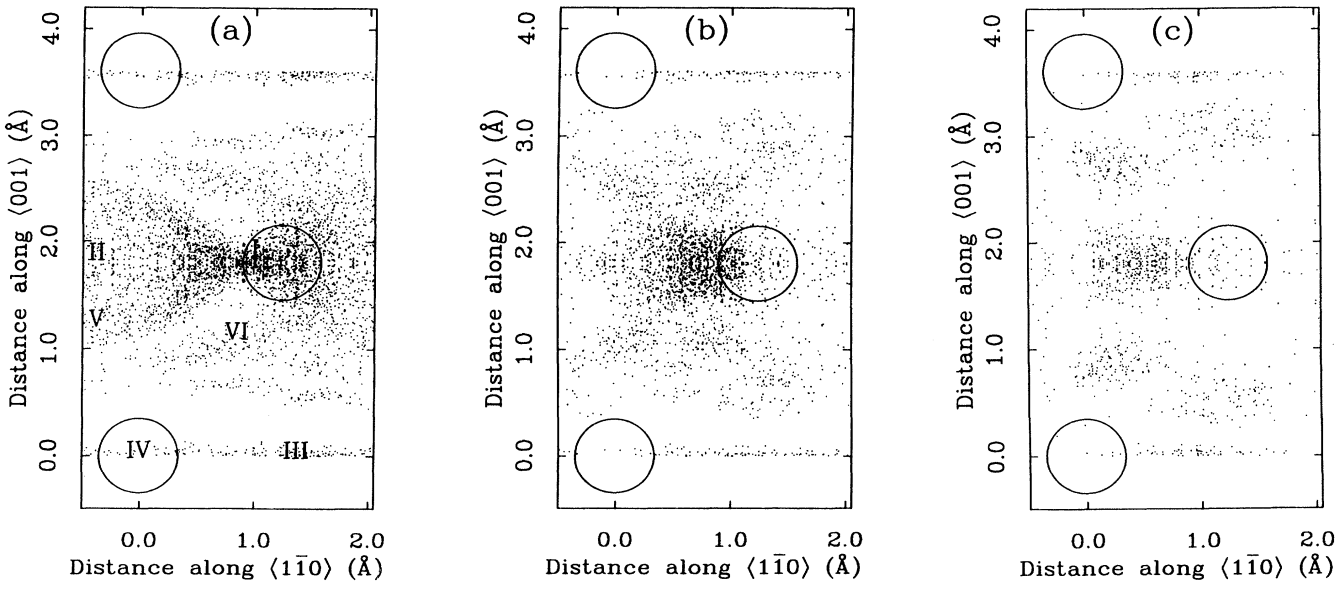

FIG. 15. Simulated impact parameter plots for a thermal surface (see text). The points correspond to impact parameters for in-plane scattered trajectories. For each impact parameter shown, its mirror image point, reflected in the plane normal to the surface and passing through the middle of the second-layer atoms, is also shown. The beam and scattering geometry are the same as for Fig. 14, and the beam energies are (a) 100 eV, (b) 200 eV, and (c) 400 eV.

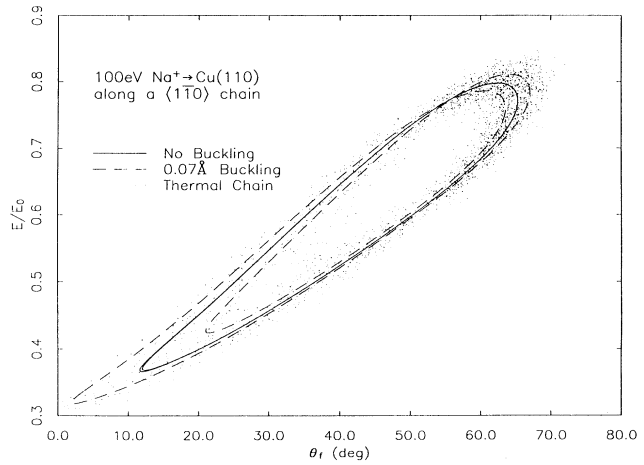

FIG. 16. Calculated E-θ loops for impact parameters along a straight and corrugated $\langle 1\bar{1}0 \rangle$ chain of Cu atoms. The corrugation is introduced by shifting every second copper atom up by 0.07 Å. The dots are the results of a thermal chain calculation (see text).

Hartree-Fock $(\text{Na-Cu})^+$ pair potentials, and a z-dependent attractive term to model the image potential. We examined the E-θ loop and the angular density distributions for this chain simulation. The calculated energy spectra showed the same general structure as the measured spectra. Full-surface thermal simulations using the Hartee-Fock pair potential accurately reproduced the final energies and angles of the scattered ions, although the peak intensities and background depended on other factors such as thermal vibrations and detector resolution.

To illustrate the sensitivity of the energy spectra to the form of the pair potential used to construct the scattering potential, we compared calculated E-θ loops using the Hartree-Fock pair potential and the pair potential of Ziegler, Biersack, and Littmarck. The calculation using the ZBL pair potential produced very different results than the HF-based simulation. In the ZBL simulations, the final scattered-ion energies were too high compared with the measured values, indicating that the pair potentials were too repulsive. This could be partially compensated for by increasing the strength of the attractive part of the potential. Even with this change, the calculated rainbow angles using the ZBL-based potential were too close together. This indicates an ion-surface interaction potential that is too smooth, and is consistent with the contribution to the ion-surface scattering potential made by the relatively large "tails" of the ZBL pair potential when summed over many adjacent surface atoms. As the beam energy is raised to 400 eV, the difference between the HF- and ZBL-based calculations decreases.

Next, to determine the relative importance of focused and zigzag collisions, we plotted the impact parameters for trajectories which can be detected in our experiments (i.e., trajectories scattered in-plane). At 100 eV, the second-layer focused trajectories dominated the scattered-ion distributions. As the energy was raised to 200 eV, the amount of focusing at the forward rainbow increased, although the focusing decreased at all other final angles. When the energy was further raised to 400 eV, the amount of focusing at all angles decreased substantially. At 400 eV, top-layer and zigzag collisions made significant contributions to the scattered-ion distributions.

The intensity maximum expected at the backward rainbow angle, which is observed in nonthermal simulations, was not seen in either our experiments or thermal simulations. Calculations showed a high sensitivity of the angular position of the backward rainbow to local variations in the geometry due to the thermal motion of the surface atoms. This is due to the closer approach of a backscattered ion to a surface atom, as compared to a forward-scattered ion. The random thermal displacements of adjacent atoms thus eliminated the intensity peak associat-

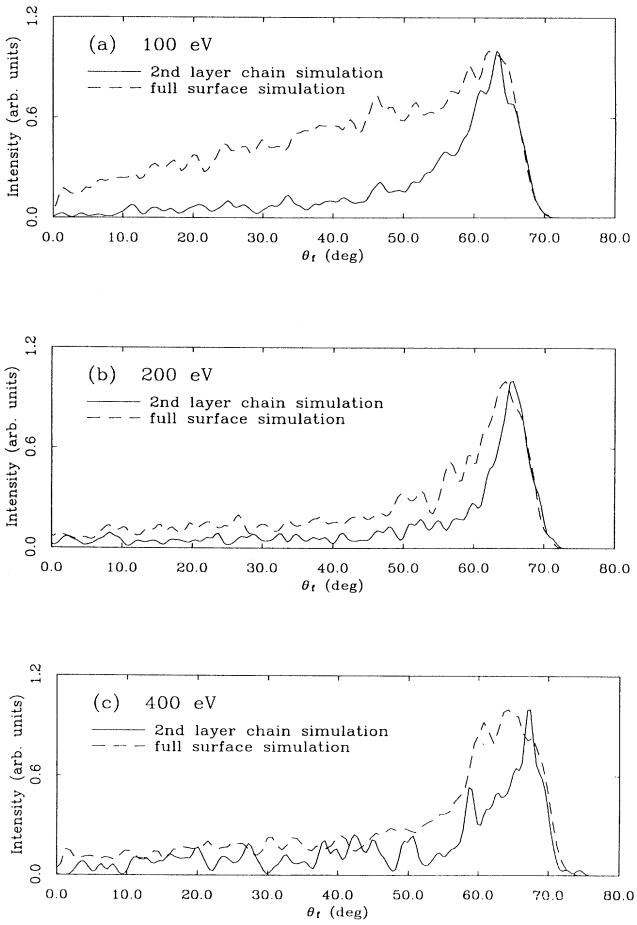

FIG. 17. Calculated angular spectra for Na^+ scattering from Cu(110) along the $\langle 1\bar{1}0 \rangle$ azimuth, for $\theta_i = 55°$. The two curves are a full-surface simulation (dashed line) and a simulation with impact parameters restricted to lie over a second-layer chain of atoms (solid line). The curves have been normalized to the forward-scattering peak. The beam energies are (a) 100 eV, (b) 200 eV, and (c) 400 eV.

ed with the backward rainbow.

Finally, we compared second-layer chain and full-surface thermal simulations. The second-layer chain simulations, which require much less computer time, produced the same values for the forward rainbow angles as the full-surface calculations. This is because most of the forward-scattered ions are focused collisions along the second-layer chain. The spectra differed at large scattering angles in the two calculations, due to the contributions of zigzag trajectories.

ACKNOWLEDGMENTS

The authors would like to acknowledge Rand McEachern and David Goodstein for their very substantial assistance with the apparatus and the simulations. Greg Kimmel and David Peale have also made contributions to the equipment. We are grateful to Ernest Behringer and Bengt Kasemo for reading the manuscript. We would also like to thank James Sethna and Stephen Holloway, whose insights have been helpful, especially with regard to the sections on thermal vibrations. D.L.A. has been supported by the National Science Foundation through the Materials Science Center (MSC) at Cornell University (Grant No. NSF-DMR-8516616). Additional support for the project has come from Grant No. NSF-DMR-8451979 and the Air Force Office of Scientific Research (Grant No. AFOSR-88-0069). The simulations were done at the Cornell MSC computing facility.

[1]W. Heiland and E. Taglauer, Nucl. Instrum. Methods **132**, 535 (1976).

[2]W. Heiland, H. G. Schäffler, and E. Taglauer, in *Atomic Collisions in Solids,* edited by S. Datz, B. H. Appelton, and C. D. Moak (Plenum, New York, 1975), Vol. 2, p. 599.

[3]A. G. J. De Wit, G. A. Van der Schootbrugge, and J. M. Fluit, Surf. Sci. **47**, 258 (1975).

[4]W. Heiland, E. Taglauer, and M. T. Robinson, Nucl. Instrum. Methods **132** 655 (1976).

[5]D. P. Jackson, W. Heiland, and E. Taglauer, Phys. Rev. B **24**, 4198 (1981).

[6]S. H. Overbury and D. R. Huntley, Phys. Rev. B **32**, 6278 (1985).

[7]M. Hou, Phys. Rev. B **136**, 7364 (1987).

[8]M. Aono, C. Oshima, S. Otani, and Y. Ishizawa, Jpn. J. Appl. Phys. **20**, 829 (1981).

[9]T. M. Buck, G. H. Weathley, and L. Marchut, Phys. Rev. Lett. **51**, 43 (1983).

[10]H. Niehus and G. Comsa, Surf. Sci. **140**, 18 (1984).

[11]E. Taglauer, Appl. Phys. A **38**, 161 (1985).

[12]Y. A. Yarmoff, D. M. Cyr, J. H. Huang, S. K. Kim, and R. S. Williams, Phys. Rev. B **33**, 3856 (1986).

[13]S. H. Overbury, Nucl. Instrum. Methods B **27**, 65 (1987).

[14]V. M. Kivilis, E. S. Parilis, and N. Yu. Turaev, Dokl. Akad. Nauk SSSR **192**, 1259 (1970) [Sov. Phys.—Dokl. **15**, 587 (1975)].

[15]B. Poelsema, L. K. Verhey, and A. L. Boers, Surf. Sci. **56**, 445 (1976); **60**, 485 (1976); **64**, 537 (1977); **64**, 554 (1977).

[16]A. L. Boers, Surf. Sci. **63**, 475 (1977).

[17]G. Engelmann, E. Taglauer, and D. P. Jackson, Nucl. Instrum. Methods B **13**, 240 (1986).

[18]See, for example, the review by J. Los and J. J. C. Geerlings, Phys. Rep. **190**, 133 (1990), and references therein.

[19]M. Hou, Vacuum **39**, 309 (1989).

[20]E. Hulpke, Surf. Sci. **52**, 615 (1975).

[21]U. Gerlach-Meyer, E. Hulpke, and H. D. Meyer, Chem. Phys. **36**, 327 (1979).

[22]E. Hulpke and K. Mann, Surf. Sci. **133**, 171 (1983).

[23]K. Mann, V. Celli, and J. P. Toennies, Surf. Sci. **185**, 269 (1987).

[24]A. D. Tenner, K. T. Gillen, T. C. M. Horn, J. Los, and A. W. Kleyn, Phys. Rev. Lett. **52**, 2183 (1984).

[25]A. D. Tenner, K. T. Gillen, T. C. M. Horn, J. Los, and A. W. Kleyn, Surf. Sci. **172**, 90 (1986); A. D. Tenner, R. P. Saxon, K. T. Gillen, D. E. Harrison, T. C. M. Horn, and A. W. Kleyn, Surf. Sci. **172**, 121 (1986).

[26]T. C. M. Horn, H. Pan, P. J. Van den Hoek, and A. W. Kleyn, Surf. Sci. **201**, 573 (1988); T. C. M. Horn, thesis, Amsterdam, 1988.

[27]R. L. McEachern, D. M. Goodstein, and B. H. Cooper, Phys. Rev. B **39**, 10 503 (1989).

[28]E. S. Parilis and N. Yu. Turaev, Dokl. Akad. Nauk SSSR **161**, 84 (1965) [Sov. Phys.—Dokl. **10**, 212 (1965)].

[29]D. P. Jackson, in *Atomic Collisions in Solids,* edited by S. Datz, B. H. Appelton, and C. D. Moak (Plenum, New York, 1975), Vol. 2, p. 599.

[30]R. P. N. Bronckers and A. G. J. De Wit, Surf. Sci. **104**, 384 (1981); **112**, 111 (1981).

[31]D. M. Goodstein, S. A. Langer, and B. H. Cooper, J. Vac. Sci. Technol. A **6**, 703 (1988).

[32]P. J. v.d. Hoek, A. D. Tenner, and A. W. Kleyn, Phys. Rev. B **34**, 5030 (1986).

[33]D. M. Goodstein, R. L. McEachern, and B. H. Cooper, Phys. Rev. B **39**, 13 129 (1989).

[34]M. J. Frisch *et al.*, GAUSSIAN86 (Carnegie-Mellon Quantum Chemistry Publishing Unit, Pittsburgh, 1984).

[35]J. P. Biersack and J. F. Ziegler, in *Ion Implantation Techniques,* edited by H. Ryssel and H. Glawischnig, Springer Series in Electrophysics Vol. 10 (Springer-Verlag, Berlin, 1982).

[36]R. L. McEachern, D. L. Adler, D. M. Goodstein, G. A. Kimmel, B. R. Litt, D. R. Peale, and B. H. Cooper, Rev. Sci. Instrum. **59**, 2560 (1988).

[37]D. L. Adler and B. H. Cooper, Rev. Sci. Instrum. **59**, 137 (1988).

[38]The sample was grown and polished by B. F. Addis of the Cornell Materials Science Department.

[39]G. A. Kimmel, D. M. Goodstein, and B. H. Cooper, J. Vac. Sci. Technol. A **7**, 2186 (1989).

[40]M. Copel, T. Gustafsson, W. R. Graham, and S. M. Yasilove, Phys. Rev. B **33**, 8110 (1986).

[41]V. M. Kivilis, E. S. Parilis, and N. Yu. Turaev, Dokl. Akad. Nauk SSSR **172**, 550 (1967) [Sov. Phys.—Dokl. **12**, 4 (1967)].

[42]V. E. Yurasova, V. I. Shulga, and D. S. Karpuzov, Can. J.

Phys. **46**, 759 (1968).
[43]E. Taglauer and W. Heiland, Surf. Sci. **33**, 27 (1972).
[44]The total scattering angle (ϑ) is related to the initial and final angles θ_i and θ_f, both measured from the surface normal, by $\vartheta = 180° - \theta_i - \theta_f$. See Fig. 2. For this paper, $\theta_i = 55°$, so $\vartheta = 125° - \theta_f$.
[45]The final energy is not exactly that predicted by the kinematic factor because of two effects: the collisions are not exactly binary, and there is an added attractive part to the potential. The former tends to raise the final energy, while the latter lowers it. See Refs. 16 and 27.
[46]Horn *et al.* (see Ref. 26) have shown that a surface scattering rainbow can be precisely defined as any final energy and direction for which the scattering cross section diverges. In this paper, however, we define the surface rainbow angles as the extreme scattering angles. These are also the angles at which the quasisingle and quasidouble scattering peaks merge. We therefore refer to the "backward rainbow," even though there may not be an associated intensity maximum observed, due to the thermal effects described in Sec. IV D.
[47]E. S. Parilis, in *Atomic Collisions Phenomena in Solids,* edited by D. W. Palmer, M. W. Thompson, and P. D. Townsend (North-Holland, Amsterdam, 1970), p. 513.
[48]Near the forward rainbow, the peak positions were determined by fitting two Gaussian curves to an energy spectrum.
[49]C. A. DiRubio (private communication).
[50]T. M. Buck, G. H. Wheatley, and L. K. Verheij, Surf. Sci. **90**, 635 (1979), and references therein.
[51]T. v. d. Hagen and E. Bauer, Phys. Rev. Lett. **47**, 579 (1981).